Facile synthesis of ZnS–Ag$_2$S core–shell nanospheres with enhanced nonlinear refraction

Azadeh Haghighatzadeh[1] [ORCID] · Mitra Kiani[1] · Babak Mazinani[2] · Joydeep Dutta[3]

Abstract

ZnS–Ag$_2$S core–shell nano/hetero-junctions have been synthesized by a two-step co-precipitation technique, in which thin layers of Ag$_2$S have been successfully coated on the surface of ZnS nanospheres. Structural studies and elemental analysis have been performed using X-ray diffraction, Fourier transfer infrared spectroscopy, field emission scanning electron microscopy, energy dispersive spectroscopy, and high-resolution transmission electron microscopy. UV–Vis diffuse reflectance spectroscopy and photoluminescence spectroscopy have been employed to investigate linear optical characteristics. Nanosecond laser pulsed-based single-beam Z-scan analysis has been used to examine the magnitude and the sign of the third-order nonlinear refractive indices. Samples show negative values of nonlinear refractive indices indicating self-defocusing optical nonlinearity under 1064 nm excitation. The results have shown that the third-order nonlinear refractive index in ZnS nanospheres can reach the magnitude of $61.0 \times 10^{-12} \mathrm{m}^2/\mathrm{W}$ by encapsulating such a nanostructure within nanometer shells of Ag$_2$S. The enhanced nonlinearity for ZnS–Ag$_2$S core–shells has been found to be 9 times higher than sole ZnS nanoparticles, which was estimated to be about $6.4 \times 10^{-12} \mathrm{m}^2/\mathrm{W}$.

1 Introduction

Third-order nonlinear optical responses of materials like third-harmonic generation (THG) and intensity-dependent refractive index variations have found applications in optical devices such as in optical switches, optical computation, optical phase conjugation, optical shutters, and information storage [1, 2]. In recent years, there has been a growing interest in the investigation of nonlinear optical properties of semiconductors as a class of materials possessing large nonlinearities and ultrafast optical response times [2]. In addition, it has been found that the reduction in the sizes of semiconductor materials from bulk to nano-sized dimensions improves nonlinear optical properties, attributed to arise due to quantum confinement [3].

Among popular nonlinear optical materials, zinc sulfide (ZnS), a group II–VI compound semiconductor, is a popular choice due to its direct band gap [4]. Stable ZnS crystals exist in cubic form (zinc blend) at room temperature and in hexagonal phases (wurtzite) at higher temperatures with band gap energies equivalent to 3.68 and 3.77 eV, respectively [5]. ZnS has been used for electro-luminescent devices, solar cells, and optical limiters as well as in optical reflectors due to its high linear refractive index and as dielectric filters due to its large optical gap [6]. ZnS shows optical nonlinearities like two-photon adsorption (TPA), second-harmonic generation (SHG), and THG that has elicited extensive interest in studying nonlinear optical behavior of ZnS nanostructures [7–9]. For example, two-photon absorption induced upon excitation with 650 nm light has been reported in ZnS nanowires prepared on Au-coated silicon substrates by a vapor phase transport (VPT) method [10]. ZnS nanostructures synthesized by laser ablation showed third-order optical susceptibility of 4.7×10^{-12} esu under 532 nm excitation [11].

Quantum-confined semiconductor nano/hetero-structures (SNHs) consisting of multiple component materials in a rationally designed spatial arrangement are promising

✉ Azadeh Haghighatzadeh
  azadeh.haghighatzadeh.physics@gmail.com

✉ Joydeep Dutta
  joydeep@kth.se

[1] Department of Physics, Ahvaz Branch, Islamic Azad University, Ahvaz, Iran

[2] Department of Materials Engineering, Malayer University, Malayer, Iran

[3] Functional Materials Group, Applied Physics Department, SCI School, KTH Royal Institute of Technology, Isafjordsgatan 22, 16440 Kista, Stockholm, Sweden

light-harvesting and charge separation materials [12]. Composite hetero-structures based on silver sulfide (Ag_2S) have been developed to improve optical and photocatalytic properties of ZnS nanostructures. Ag_2S has a direct band gap with a narrow band of about 1.1 eV in bulk crystals, which can be effectively increased with size reduction of the crystallites [13]. Ag_2S has found application in electro-optical industry due to its extensive use as photoconductors, in infrared detectors and as light sensitizers [14]. Kaur et al. have synthesized ZnS–Ag_2S nanocomposites via a chemical precipitation route and investigated optical and photocatalytic characteristics [12]. Kumar et al. prepared visible-light-active nano-sized Ag_2S–ZnS loaded on cellulose by a precipitation method and studied photocatalytic degradation of rhodamine B dye [15]. From the viewpoint of nonlinear optics, Ag_2S can be considered as an appropriate candidate to enhance optical nonlinearities in ZnS nanostructures due to nonlinear features such as two-photon absorption and nonlinear refractive index, which have been demonstrated at 532 nm [16].

The construction of core–shell hetero-structures possessing integrated characteristics of disparate components can be a desired strategy for practical applications of nonlinear optical materials. Such a heterostructure not only exhibits unique multi-functionalities but also withholding basic features of the individual components [17]. Despite outstanding nonlinear properties of ZnS and Ag_2S semiconductors, a limited number of reports have been published to investigate nonlinear optical characteristics of ZnS–Ag_2S-based core–shell nanostructures. Dehghanipour et al. prepared particles with Ag_2S cores coated with ZnS shells via a one-pot pulsed microwave irradiation and reported optical nonlinearities at an excitation wavelength of 532 nm [18]. Liu et al. investigated nonlinear optical properties of near-infrared region Ag_2S quantum dots pumped by 532 nm nanosecond laser pulses [19]. Although many researchers have focused on ZnS–Ag_2S core–shell structures, there are no reports investigating optical nonlinearities of ZnS nanoparticles encapsulated by Ag_2S layers.

The present study focuses on the synthesis of a well-engineered ZnS–Ag_2S core–shell structure through a two-step co-precipitation process and studies on the third-order nonlinear refractive index changes. The successful construction of ZnS–Ag_2S core–shells in this work can be considered as a significant achievement because the synthesis of uniform Ag_2S shells on the surface of ZnS particles has been a challenge due to the tendency of Ag_2S clusters to aggregate into bulk structures [20]. Furthermore, to the best of our knowledge, optical nonlinearities of ZnS and Ag_2S-based nanostructures have not yet been examined in the near-infrared region (1064 nm).

2 Experimental

2.1 Chemicals

Sodium sulfide hydrate ($Na_2S \cdot nH_2O$, 60.0–62.0%, $M_W = 78.04$) was purchased from Gyeonggi-do, South Korea. Silver nitrate ($AgNO_3$, $M_W = 166.78$), zinc acetate dehydrate ($Zn(CH_3COO)_2 \cdot 2H_2O$, $M_W = 219.49$), ethylenediaminetetraacetic acid (EDTA, $M_W = 372.24$, purity > 98%), thioglycolic acid (TGA, $C_2H_4O_2S$, $M_W = 92.11$, purity > 98%), acetone (C_3H_6O, $M_W = 58.08$), and ammonium hydroxide (NH_4OH, $M_W = 35.04$) were procured from Merck and used as received without further purification. Deionized water was used for all the experiments.

2.2 Preparation of ZnS core nanostructures

Nanocrystalline ZnS was synthesized by a wet chemical precipitation method from zinc acetate [$Zn(CH_3COO)_2 \cdot 2H_2O$] and sodium sulfide [$Na_2S \cdot nH_2O$] as zinc and sulfur sources, respectively. Figure 1a schematically shows the procedure followed for ZnS nanoparticles (NPs) synthesis. In a typical experiment, 1.09745 g of zinc acetate was dissolved in 50 mL deionized water followed by the additions of EDTA as a capping ligand and ammonia to control the pH. In a separate beaker, 12.79 g of sodium sulfide was dissolved in 50 mL deionized water and then the resultant solution was added into an acidic solution of zinc acetate under vigorous magnetic stirring at room temperature for 2 h. The final precipitate was collected by centrifugation at a speed of 3000 rpm for 10 min, washed several times with acetone and finally dried in an atmospheric oven at a temperature of 100 °C for 20 h.

2.3 Preparation of ZnS–Ag_2S core–shell nanoheterojunctions

ZnS–Ag_2S core–shell nano/hetero-junctions (CSNHs) were successfully synthesized by a facile co-precipitation deposition method. Schematic illustration of the fabrication of ZnS–Ag_2S CSNHs is shown in Fig. 1b. To prepare CSNHs, 0.4 g of silver nitrate ($AgNO_3$) as a source of silver accompanied by TGA as a capping agent was dissolved in 50 mL deionized water and continuously stirred for 20 min. 7.7476 g of sodium sulfide was separately dissolved in 75 mL deionized water and then added to the above solution. Ammonia was also added to the reaction solution to adjust the desired pH resulting in the formation of a transparent solution. In order to complete the synthesis process of ZnS–Ag_2S CSNHs, 0.2 g of the as-prepared ZnS NPs was dispersed in 20 mL deionized water for 30 min and

Fig. 1 Schematic illustration of synthesis procedure for **a** ZnS NPs and **b** ZnS/Ag$_2$S CSNHs
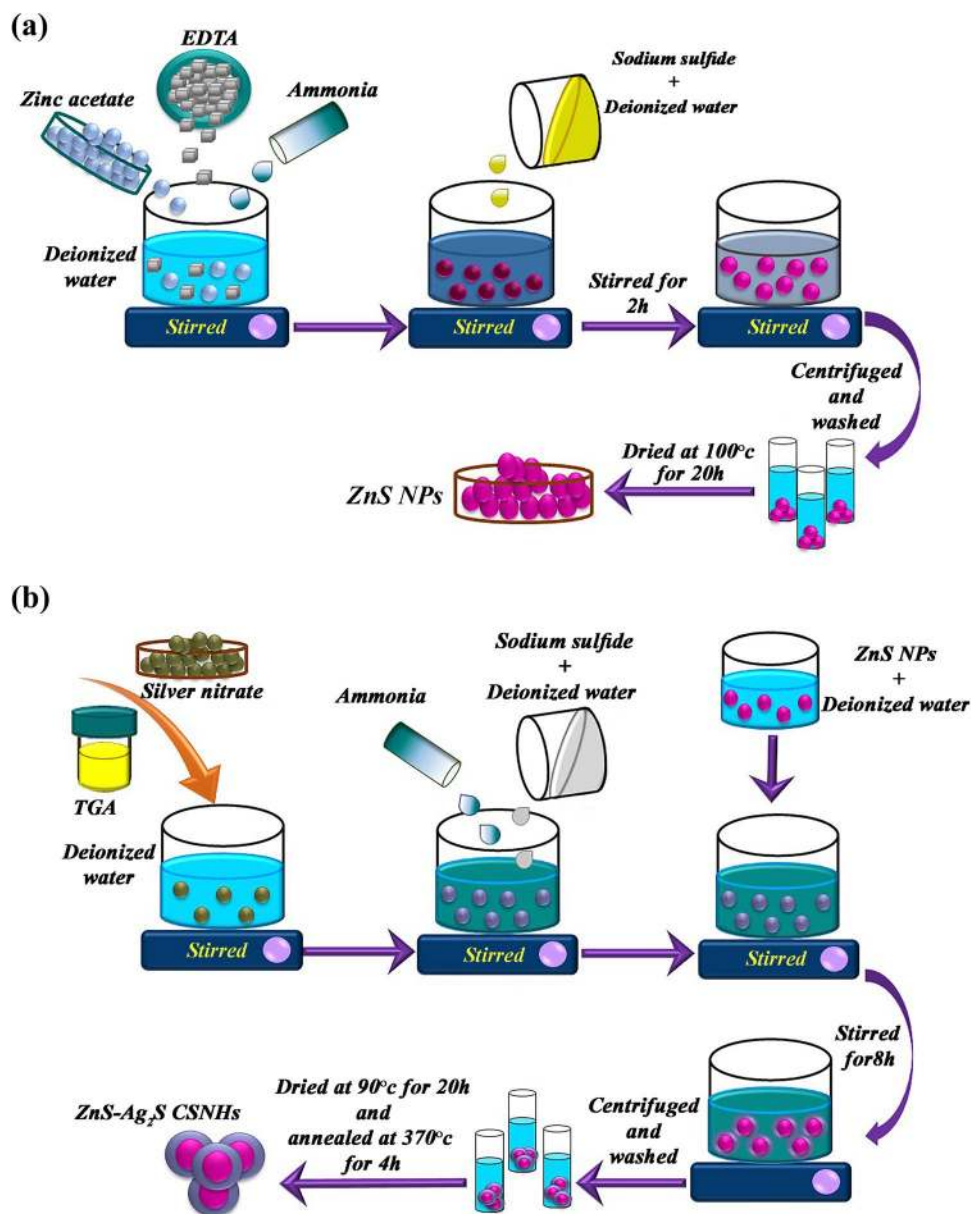
then added into the prepared growth solution for the Ag$_2$S shell. After a waiting period of 8 h for the completion of the reaction under constant stirring at room temperature, the obtained product was collected by a multiple rinse-centrifugation process with acetone. The final product was dried at 90 °C for 20 h and annealed at 370 °C for 4 h in air yielding ZnS–Ag$_2$S CSNHs.

2.4 Characterization techniques

X-ray diffraction (XRD) analysis was performed to investigate crystalline phases using an Ultimate IV Multipurpose X-ray diffractometer with Cu K$_\alpha$ ($\lambda = 0.15406$ nm) radiation. X'Pert HighScore Plus Software was used to analyze the diffractograms. Fourier transform infrared (FT-IR) spectra were measured to analyze chemical structures of samples by a Perkin Elmer BX-II FT-IR spectrophotometer. Surface morphology was observed using field emission scanning electron microscopy (FESEM, Zeiss SIGMA VP-500), equipped with an energy dispersive spectroscopy (EDS) detector (SAMAX) to characterize elemental compositions. Further microstructure information was obtained through high-resolution transmission electron microscopy (HRTEM, JEM 2100, JEOL). Ultraviolet–Visible diffuse reflectance spectra (DRS) were recorded with a UV–Vis spectrophotometer (Avaspec-2048-TEC). Photoluminescence (PL) spectra were measured utilizing a Perkin Elmer LS55 fluorescence spectrophotometer with excitation wavelength of 250 nm.

2.5 Nonlinear optical measurements

The nonlinear optical behavior of the synthesized nanostructures was analyzed using the standard single-beam Z-scan technique. In order to provide a reasonable comparison between the nonlinear optical response of Pristine–ZnS NPs and ZnS–Ag$_2$S CSNHs, both samples were tested under the same experimental conditions. A specific concentration of nanostructures was dispersed in deionized water and poured into a quartz cell of 1 mm thickness. Figure 2 shows the schematic configuration of the Z-scan arrangement employed to measure the third-order nonlinear refractive index. A pulsed Nd-YVO$_4$ laser operating at a wavelength of 1064 nm with a radiance power of 63 mW was used as the light source. The duration of the laser pulse with a repetition rate of 10 kHz was 50 ns. As shown in Fig. 2, the propagation direction was considered as the z-axis (optical axis) in the right-handed standard coordinate system where entrance and exit faces of optical elements were placed on the x–y plane. Light emitted from the laser source was first split into two parts by B_1 beam splitter. One part as the reference signal was detected by the D_1 photodetector to record pulse-to-pulse fluctuations, while the other part of the excitation beam was focused on samples through a 300-mm focal-length lens. The samples were translated along the optical axis by a motorized transition stage in 0.5 mm steps in the region including the lens focal plane.

A control experiment was simultaneously conducted using the B_2 beam splitter to eliminate the possible effects which may arise due to nonlinear absorption phenomenon. As illustrated in Fig. 2, B_2 beam splitter guided the light beam transmitted from samples towards D_2 and D_3 photodetectors in closed and open-aperture Z-scan arrangements to examine nonlinear absorption and refraction characteristics, respectively. D_2 photodetector recorded the power transmitted from samples after passing through a transmittance aperture $S = 0.13$ as a function of the sample position. Results obtained from the D_2 photodetector were then divided by open-aperture transmittances detected by the D_3 photodetector to minimize the nonlinear absorption. The effects due to pulse-to-pulse fluctuations were also reduced by normalizing with signals detected using the D_1 reference photodetector.

Transmittance obtained for a z position was finally normalized to the transmittance of the Rayleigh length $\left(z_0 = \pi/\omega_0^2\lambda\right)$ as $T\left(z/z_0\right) \cong I(z)/I(\infty)$, where $I(z)$ is the intensity recorded in the coordinate z and $I(\infty)$ is for the position where the sample was located far away from the focus of the lens [21]. A nonlinear sample acting as a positive lens tends to collimate the laser beam, showing the self-focusing effects. Such a self-focusing behavior can be seen with the emergence of a pre-focal valley followed by a post-focal peak. However, self-defocusing effects appear in samples with a negative nonlinearity and show a pre-focal peak and a post-focal valley in their transmittance curves with respect to z-axis [22].

In the absence of nonlinear absorption, the third-order nonlinear refractive index (n_2) can be approximated by the following theoretical relation [23]:

$$\Delta T_{PV} = 0.406(1 - S)^{0.27}\left(2\pi/\lambda\right)n_2 I_0 L_{eff}, \tag{1}$$

where $\Delta T_{PV} = T_P - T_V$ stands for the transmittance difference between the peak and valley when T_P and T_V are considered as the normalized peak and valley transmittances, respectively. $I_0 = 1.25 \times 10^7 W/m^2$ refers to the incident intensity of laser beam at the focus and L_{eff} is the effective length of the sample and is determined as follows [24]:

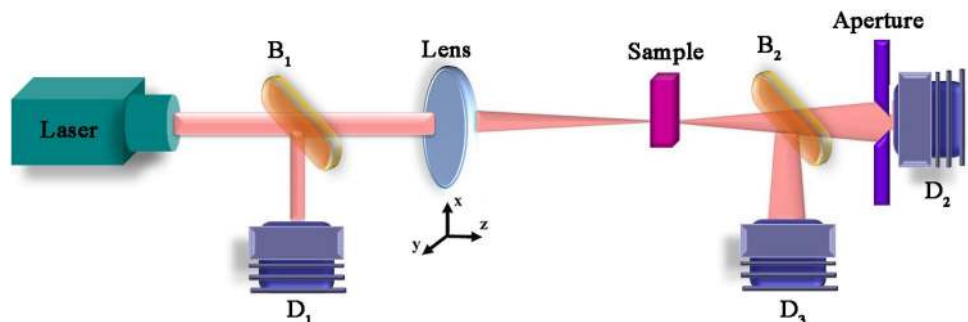$$L_{eff} = \frac{1 - \exp(-\alpha L)}{\alpha}, \tag{2}$$

where α is a linear absorption coefficient and L is the sample thickness.

3 Results and discussions

3.1 XRD analysis

Figure 3 shows the XRD patterns of Pristine–ZnS NPs and ZnS–Ag$_2$S CSNHs with a 2θ scanning angle ranging

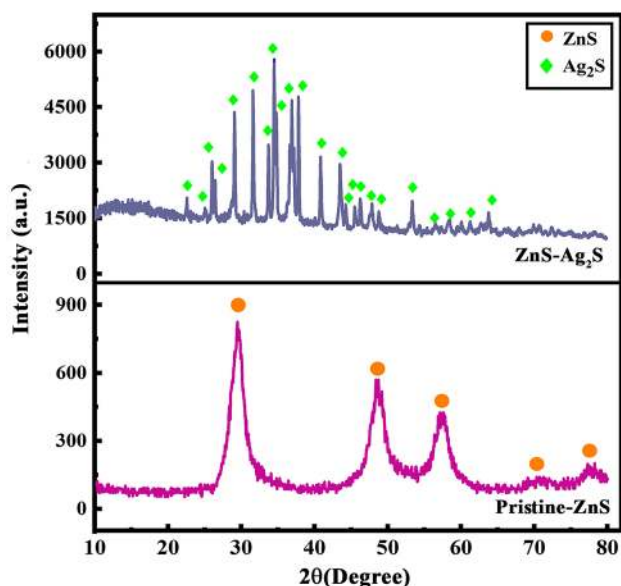**Fig. 2** Block diagram of experimental arrangement for Z-scan setup

Fig. 3 XRD patterns for Pristine–ZnS NPs and ZnS–Ag$_2$S CSNHs

from 20° to 80°. Five characteristic diffraction peaks were observed in the Pristine–ZnS samples at 29.4°, 48.5°, 57.3°, 70.8°, and 77.2°, which can be indexed to the (111), (220), (311), (400), and (331) planes of cubic ZnS (JCPDS No. 79-0043). No other impurities could be detected in Pristine–ZnS diffractograms, confirming the high purity of the synthesized ZnS NPs. XRD pattern of ZnS–Ag$_2$S CSNHs can be referred to the structure of monoclinic Ag$_2$S according to the standard card (JCPDS No. 14-0072). For ZnS–Ag$_2$S CSNH sample, diffraction peaks appeared at 2θ values of 22.5°, 25.0°, 26.0°, 26.3°, 29.0°, 31.6°, 33.7°, 34.4°, 34.7°, 36.9°, 37.8°, 40.9°, 43.4°, 44.2°, 45.5°, 46.2°, 47.8°, 48.8°, 53.3°, 56.5°, 58.4°, 61.2°, and 63.8° that can be ascribed to the (10$\bar{1}$), (110), (11$\bar{1}$), (01$\bar{2}$), (111), (11$\bar{2}$), (120), (12$\bar{1}$), (022), (121), (10$\bar{3}$), (031), (200), (103), (13$\bar{1}$), (12$\bar{3}$), (21$\bar{2}$), (211), (22$\bar{2}$), (114), (04$\bar{2}$), (14$\bar{2}$), and (13$\bar{4}$) planes. No obvious characteristic peaks related to cubic ZnS phases can be found in ZnS–Ag$_2$S CSNHs. The absence of diffraction peaks relevant to cubic ZnS NPs in the XRD pattern of ZnS–Ag$_2$S CSNHs might be attributed to arise due to overlapping peaks of ZnS (111), (220), and Ag$_2$S (111), (211) [25].

3.2 FT-IR analysis

FT-IR spectrum of Pristine–ZnS NPs shows absorption bands situated at 495.16 and 626.20 cm^{-1} that is assigned to Zn–S vibration [26]. The sharp adsorption band centered at 998.40 cm^{-1} can be attributed to the resonance interaction between vibrational modes of sulfide ions in ZnS crystal [27]. The bands appearing at 1416.77 and 1585.71 cm^{-1} correspond to the stretching modes of carboxyl (C=O)
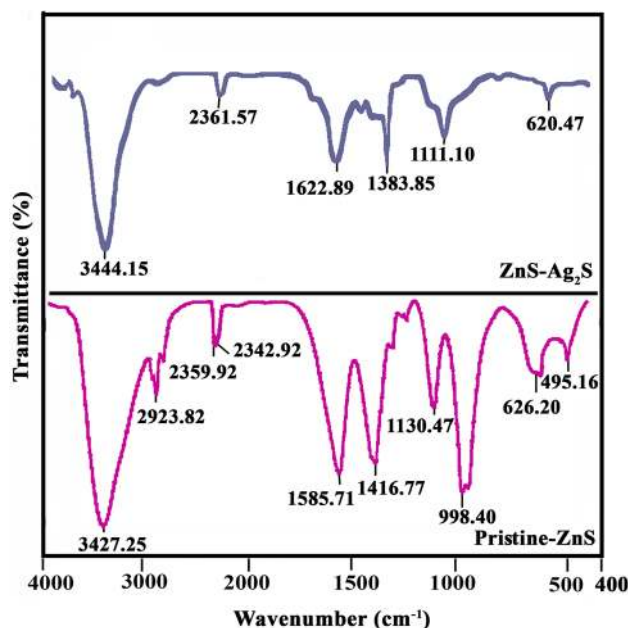

Fig. 4 FT-IR spectra for Pristine–ZnS NPs and ZnS–Ag$_2$S CSNHs

groups arising from atmospheric CO$_2$ adsorbed on the ZnS surface [28]. The bands located at 2342.93, 2359.92, and 2923.82 cm^{-1} might originate from microstructure formation of Pristine–ZnS NPs [26]. The broad and strong band observed around 3427.25 in the FT-IR spectrum of Pristine–ZnS NPs is from O–H stretching modes, arising from the water adsorbed on the ZnS surface via –COOH group [28]. As shown in Fig. 4, the FT-IR spectrum of ZnS–Ag$_2$S CSNHs show a typical absorption peak at 620.47 cm^{-1} corresponding to Ag–N vibrations [29]. In addition, absorptions at 1111.10 and 1383.85 cm^{-1} can be ascribed to C–O and C=O stretching vibrations, respectively [25]. The absorption peak located at 1622.89 cm^{-1} and the weak band at 2361.57 cm^{-1} can belong to aromatic C=C band [25] and microstructure formation of the sample [26], respectively. The broad adsorption peak centered around 3444.15 cm^{-1} corresponds to O–H group from water molecules adsorbed on the surface of CSNHs [26].

3.3 FESEM–EDS analysis

Figure 5 shows the FESEM images captured in two different magnifications for Pristine–ZnS NPs and ZnS–Ag$_2$S CSNHs. Pristine–ZnS sample exhibits a regular shape with aggregations of many nearly spherical particles, which possess dimensions ranging from 16 to 30 nm (Fig. 5a, b). The enlarged view of Pristine–ZnS NPs (Fig. 5b) further reveals an almost rough surface morphology due to assimilation of nanoparticles. FESEM images of samples after the growth of Ag$_2$S nanostructures are shown in Fig. 5c, d. It is obvious

Fig. 5 FESEM images of **a, b** Pristine–ZnS NPs and **c**, **d** ZnS–Ag$_2$S CSNHs in **a**, **c** low and **b**, **d** high magnifications; Insets: corresponding EDS spectra
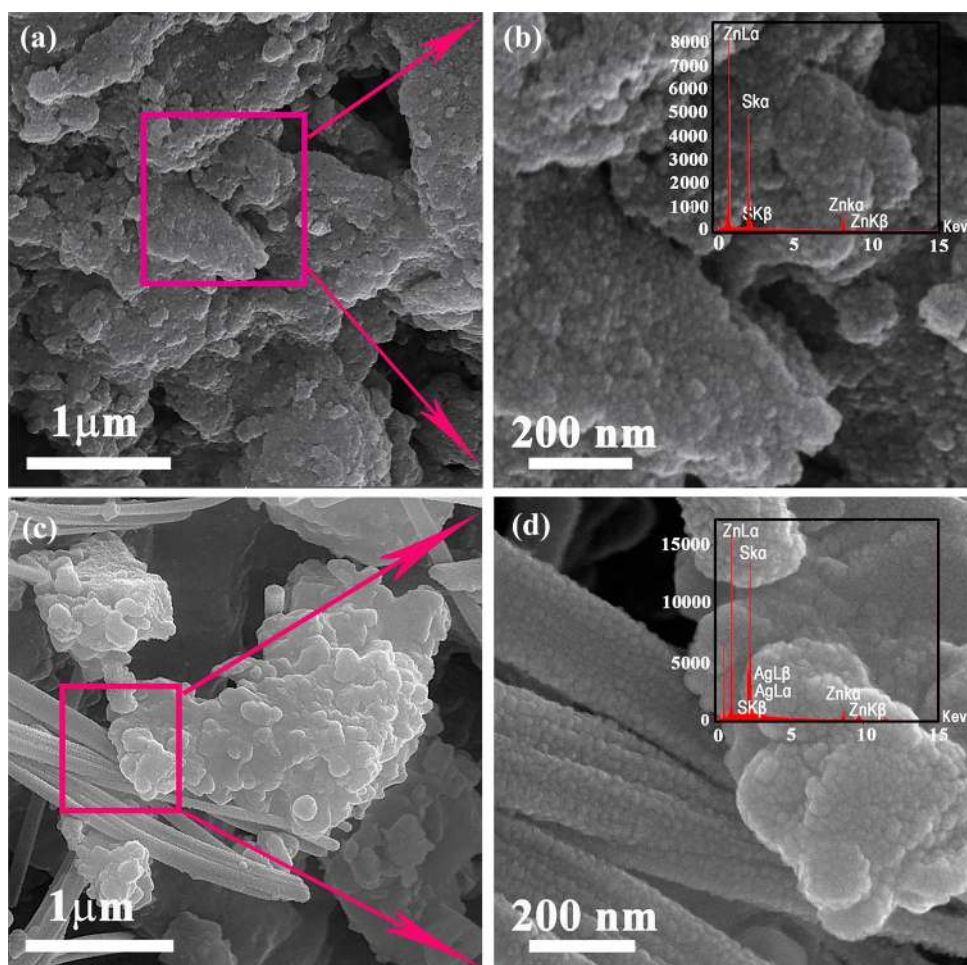

Table 1 Quantitative EDS analysis of Pristine–ZnS and ZnS–Ag$_2$S samples

Sample	Zn (wt%)	S (wt%)	Ag (wt%)
Pristine–ZnS	27.06	77.94	–
ZnS–Ag$_2$S	11.37	81.84	6.79

from Fig. 5c, d that ZnS–Ag$_2$S CSNHs consists of spherical-shaped smooth morphology in the size ranges of 20–80 nm. It can be also concluded from Fig. 5d that the rod-like shapes formed in FESEM images relevant to ZnS–Ag$_2$S CSNHs are due to the agglomerated spheres.

EDS spectra obtained for Pristine–ZnS NPs and ZnS–Ag$_2$S CSNHs are shown as insets in Fig. 5b and d, respectively. The results confirm the presence of zinc (Zn) and sulfur (S) elements in EDS spectrum of Pristine–ZnS NPs and of Zinc (Zn), sulfur (S), and silver (Ag) in that of ZnS–Ag$_2$S CSNHs without any detectable traces of other impurities. The numerical values related to atom percentages of the constituent elements are summarized in Table 1. The states of surface element dispersion for ZnS–Ag$_2$S CSNHs

are further analyzed by the elemental mapping technique and results are presented in Fig. 6. The elemental maps (Fig. 6b–d) for the surface region (Fig. 6a) suggest homogeneous distributions of Zn, S, and Ag elements in ZnS–Ag$_2$S CSNHs.

3.4 HRTEM analysis

In order to study the core–shell structures of the as-synthesized ZnS–Ag$_2$S samples, high-resolution transmission electron microscopy (HRTEM) was used. A typical HRTEM image of an individual ZnS–Ag$_2$S nanostructure is shown in Fig. 7, clearly revealing a core–shell structure of ZnS–Ag$_2$S sample, displaying a darker core (ZnS) surrounded by a lighter thin layer as a shell (Ag$_2$S). Careful analysis of the image shows Ag$_2$S shell thickness of ~ 5.8 nm around a spherical core of ZnS with a diameter ~ 80 nm.

3.5 UV–Vis diffuse reflectance spectroscopy (DRS)

Light absorbance of Pristine–ZnS NPs and ZnS-Ag$_2$S CSNHs measured in a wavelength range of 200–800 nm is
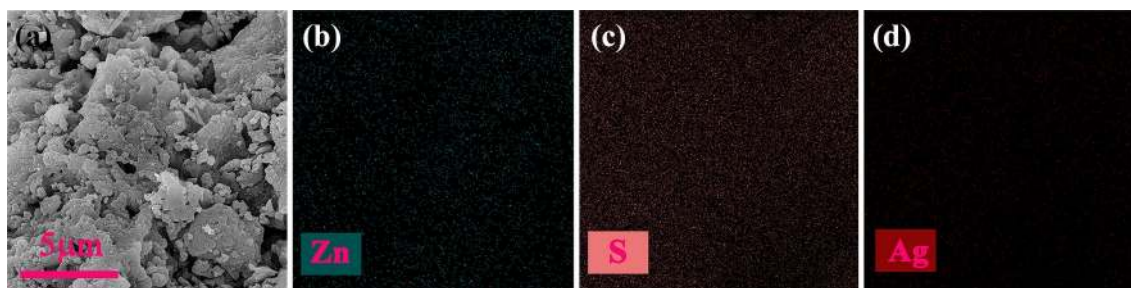
Fig. 6 **a** FESEM map image and **b**–**d** corresponding elemental mappings of ZnS–Ag$_2$S CSNHs

Fig. 7 HRTEM image of ZnS–Ag$_2$S CSNHs
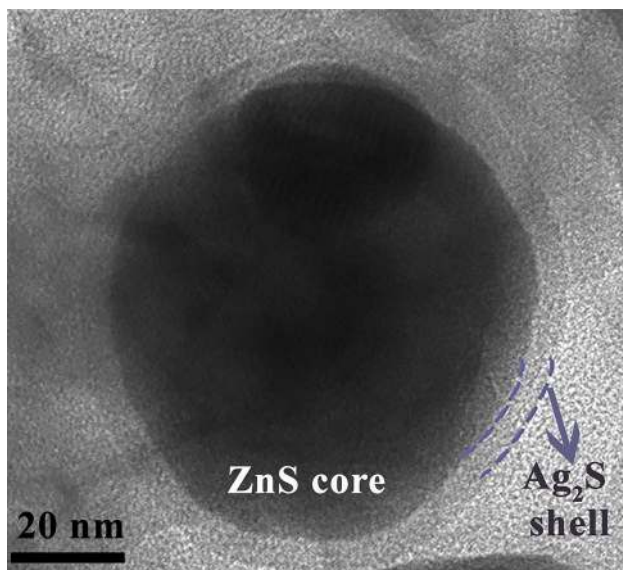

Fig. 8 UV–Vis absorption spectra of Pristine–ZnS NPs and ZnS–Ag$_2$S CSNHs

shown in Fig. 8. Pristine–ZnS NPs shows a relatively strong absorption in the wavelength range of 250–350 nm. It is obvious from Fig. 8 that ZnS NPs after being encapsulated in Ag$_2$S nanocrystals demonstrate enhanced absorption in the visible region as compared to Pristine–ZnS NPs. However, the light absorption in ZnS–Ag$_2$S CSNHs is weakened in the UV region due to the presence of Ag$_2$S layers around ZnS nanocrystals. Shells of Ag$_2$S nanostructures with near-infrared optical gap and intrinsically large absorption coefficient, forming on the surface of ZnS NPs, prevent direct penetration of UV radiation into ZnS structures resulting in a comparatively lower absorption in the UV region [12]. The results indicate that an increase in visible light absorbance for ZnS NPs can successfully occur by encapsulating such a nanostructure coated with layers of Ag$_2$S nanocrystals.

3.6 Photoluminescence (PL) spectroscopy

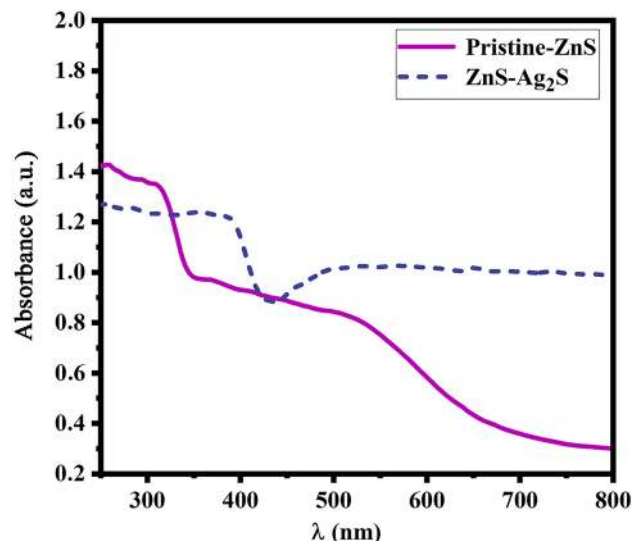The room-temperature PL spectra of the as-synthesized samples were recorded in a wavelength range of 300–800 nm

under an excitation wavelength of 250 nm (4.96 eV) as shown in Fig. 9a. It is obvious from Fig. 9a that Pristine–ZnS NPs show two similarly broad emission bands located around ~ 400 nm (3.1 eV) and ~ 680 nm (1.82 eV). The first band ranges from 300 to 550 nm with full width at half maximum (FWHM) of 128 nm, while the second band spreads from 650 to 800 nm with a FWHM of 130 nm. Photophysical processes describing the possible emission mechanisms of Pristine–ZnS NPs (Fig. 9b) suggest several possible recombination pathways of the photo-excited excitons. The proposed electronic transitions are the results of defects, which are formed during the growth process of Pristine–ZnS NPs. The structural defects in Pristine–ZnS NPs comprise point, line, and plane defects. The line and plane defects cannot participate in emission processes due to the lack of the quantum confinement effects [30]. Therefore, the presence of emission centers activated in Pristine–ZnS NPs probably originates only from point defects such as Scottky defects (vacancy states) and Frenkel defects (interstitial states) [12, 30]. Zinc interstitial atoms and sulfur vacancies lie in the
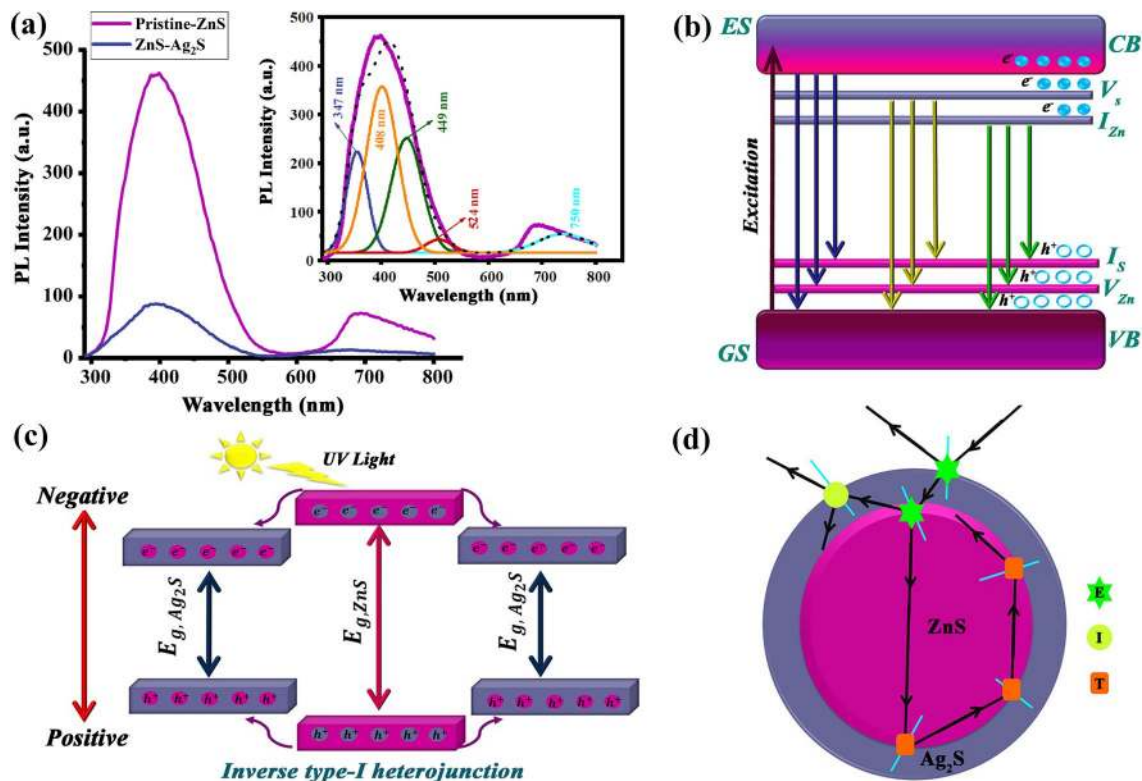
Fig. 9 a Photoluminescence emission spectra of Pristine–ZnS NPs and ZnS–Ag$_2$S CSNHs. Inset: Multi-peak Gaussian fit of Pristine–ZnS , **b** schematic representation of the emission mechanism in Pristine–ZnS NPs (*CB* conduction band, *VB* valence band, *ES* excited state, *GS* ground state, *V$_S$* sulfur vacancies, *V$_{Zn}$* zinc vacancies, *I$_S$* sulfur interstitials, *I$_{Zn}$* zinc interstitials), **c** illustration of the band alignment and the charge-transfer process in ZnS–Ag$_2$S CSNHs, and **d** transmissions paths of a light ray as it enters a ZnS–Ag$_2$S CSNH nanosphere (*E* external reflection, *I* internal reflection, *T* total internal reflection)

ZnS forbidden gap and close to the conduction band to act as donor energy states. However, sulfur interstitial atoms and zinc vacancies lead to acceptor levels located above the valence band of Pristine–ZnS NPs [12, 25].

Based on the schematic illustration as in Fig. 9b, in addition to relaxation paths relevant to photo-excited electrons from the conduction band to the valence band and accepter levels formed in the forbidden region, there is a possibility for the recombination of electrons to be trapped in donor levels with photo-excited holes in the valence band and also holes trapped in acceptor states. Therefore, the extended emission pattern of Pristine–ZnS NPs confirms the presence of multiple point defect states in the ZnS nanostructures. A careful survey with a multi-peak Gaussian fit illustrated as an inset in Fig. 9a suggests that the first emission band from Pristine–ZnS NPs could be ascribed to arise from band-to-band emission and defect states including sulfur interstitials, sulfur vacancies, and zinc interstitials, which can be resolved into four Gaussian curves centered at 347, 408, 449, and 524 nm, respectively [25, 31]. However, deep level zinc vacancies are commonly considered to be responsible for a Gaussian emission spectrum centered at 750 nm [31] that appears at the second emission band related to Pristine–ZnS

sample. It is noteworthy that the overall theoretical fit estimated in inset of Fig. 9a (dotted curve) comprising five overlapped peaks is in good agreement with experimental observations for Pristine–ZnS NPs.

For comparison, Fig. 9a displays emission patterns relevant to both Pristine–ZnS and ZnS–Ag$_2$S samples. It is also clear from Fig. 9a that ZnS–Ag$_2$S CSNHs show a significant decrease in the excitonic PL intensity after the growth of Ag$_2$S shells on the surface of ZnS nanostructures. This could arise from enhanced charge separation due to the coupling of ZnS and Ag$_2$S nanostructures as well as due to passivation of surface defects. A schematic diagram of electron–hole separations at the interface of ZnS–Ag$_2$S CHNHs is proposed in Fig. 9c. The core–shell heterojunction (Fig. 9c) follows an inverse type-I scheme [32] where the conduction band of ZnS is located at a more negative potential compared to that of Ag$_2$S, while its valence band is more positive than that of Ag$_2$S [33]. Because electrons and holes tend to migrate, due to the less negative conduction band and the less positive valence band at a semiconductor/semiconductor interface, respectively [34], both electrons and holes are transferred to Ag$_2$S shell region. In the inverse type-I ZnS–Ag$_2$S CSNHs, the charge carriers are partially spread within the Ag$_2$S

shells, lowering the probability of charge recombination in ZnS cores. Subsequently, a weaker PL signal is expected for ZnS–Ag$_2$S CSNHs compared to Pristine–ZnS NPs. On the other hand, the presence of Ag$_2$S layer on the surface of ZnS core passivates the emission from surface defects of ZnS, which in turn leads to dominating emission characteristics relevant to Ag$_2$S shell in the emission pattern of ZnS–Ag$_2$S CSNHs. Weak emission intensities for Ag$_2$S nanostructures compared to those of ZnS nanostructures have been reported by many researchers, which may be ascribed to the low light emission time span due to the smaller band gap [35]. The weak PL emission may also originate from the thin Ag$_2$S coating on the ZnS surface lowering optical absorption of excitation photons. A similar trend has also been observed for hollow ZnS/Ag$_2$S core/shell nanospheres as compared to hollow ZnS nanoparticles alone [35]. Reddy et al. have also reported lower PL intensity for ZnS–Ag$_2$S nanocomposites compared to ZnS nanostructures [25]. In addition, the lower PL intensity may be explained by multiple reflections, due to the Ag$_2$S shell overlayers. Since the Ag$_2$S shell has a smaller refractive index (2.2) than that of the ZnS core (2.35) [36], Ag$_2$S shell can act as an antireflection layer and confine light rays into the ZnS core [37]. An illustration of possible reflection mechanisms in the interfaces of ZnS–Ag$_2$S CSNHs is suggested in Fig. 9d. It is concluded from Fig. 9d that because of sequential total internal reflections at the interface of the Ag$_2$S shell and the ZnS core, most of the light is absorbed by ZnS nanostructures, which is evident because of the thickness of the shell.

3.7 Z-scan analysis

In Fig. 10, we have plotted the normalized results obtained from the division of the closed-aperture Z-scan data by the open-aperture Z-scan data for Pristine–ZnS NPs and ZnS–Ag$_2$S CSNHs indicating that both divided Z-scan traces exhibit a pre-focal peak followed by a post-focal valley. The resultant peak-valley shapes confirm the presence of the third-order nonlinear refractive indices for both Pristine–ZnS and ZnS–Ag$_2$S samples. The peak-valley configuration shaped in the vicinity of the focus ($z = 30$ cm) reveals the self-defocusing effects relevant to negative lens effects for such intensity-dependent refractive indices.

Due to the lack of linear absorption ($\alpha \approx 0$) in Pristine–ZnS NPs and ZnS–Ag2S CSNHs for the applied wavelength (1064 nm), differences in the magnitude of the nonlinear refractive indices can be directly calculated from the transmittance differences created between the peak and valley (Eq. 1). Therefore, it can be found from Fig. 10 that the nonlinearity of ZnS NPs indicates a remarkable enhancement in the samples encapsulated by a Ag$_2$S shell. The third-order nonlinear refractive indices of samples tested are calculated from Eq. (1) and the results are summarized in Table 2. An increase in the
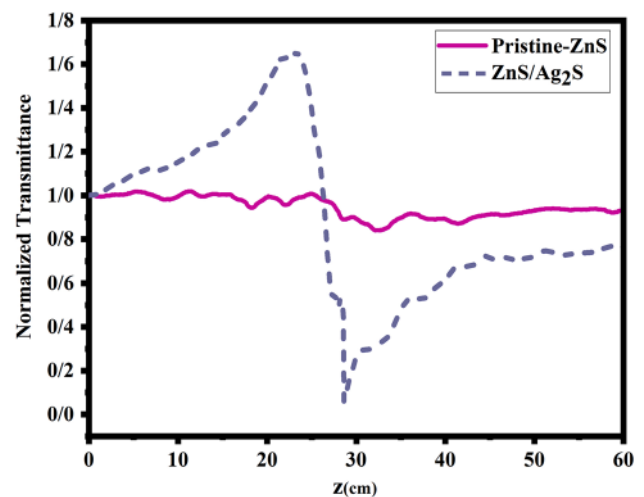

Fig. 10 Normalized Z-scan traces of Pristine–ZnS NPs and ZnS–Ag$_2$S CSNHs resulting from closed-aperture data divided by open-aperture data

Table 2 The results of the third-order nonlinear refractive measurements of Pristine–ZnS and ZnS–Ag$_2$S samples

Sample	T_P	T_V	ΔT_{PV}	n_2 (m^2/W)
Pristine–ZnS	1.007	0.839	0.168	6.4×10^{-12}
ZnS–Ag$_2$S	1.654	0.06	1.593	61.0×10^{-12}

nonlinear refractive index of ZnS NPs covered by Ag$_2$S shells increased from 6.4×10^{-12} m^2/W to 61.0×10^{-12} m^2/W, which is more than nine times higher than that of Pristine–ZnS NPs. This improvement in the resultant third-order refractive index can be understood by considering the effect of the Ag$_2$S shell growth on ZnS cores. It is noteworthy to point out that nonlinear refractive indices of Ag$_2$S cores covered by ZnS shells have been previously reported to be in the range of 0.93×10^{-9} cm^2/W to 9.16×10^{-9} cm^2/W under excitation of 532 nm, which are relatively small compared what is obtained in this work [38]. However, the third-order refractive indices estimated in this study are comparable to that of Ag/TiO$_2$ core/shell nanostructures ($\sim 40.21 \times 10^{-12}$ m^2/W) measured at 532 nm [39]. In addition, similar values with a magnitude of 1.1×10^{-12} m^2/W have been obtained for the nonlinear optical response of reduced graphene oxide decorated with silver nanoparticles at 800 nm [2].

4 Conclusions

The co-precipitation synthesis of ZnS–Ag$_2$S CSNHs via a two-step process has been reported in this work. The as-synthesized ZnS–Ag$_2$S CSNHs have been characterized using

a series of techniques including XRD, FT-IR, SEM, EDS, and HRTEM. XRD and EDS-FESM confirm the formation of cubic ZnS and monoclinic Ag_2S phases in the core and shell nanostructures, respectively. Morphological studies have demonstrated spherical-like core–shell nanostructures, in which ZnS spheres with a diameter of about 80 nm are coated with Ag_2S layers having a thickness of about 5.8 nm. Spectral characteristics of nanostructures have been examined by UV–Vis DRS and PL analyses. $ZnS–Ag_2S$ CSNHs show a stronger adsorption shift towards larger wavelengths of electromagnetic spectrum compared to the Pristine–ZnS NPs. PL analysis under an excitation of 250 nm revealed the formation of vacancy and interstitial states of zinc and sulfur atoms in the structure of synthesized nanospheres. Nonlinear optical properties of Pristine–ZnS NPs and $ZnS–Ag_2S$ CSNHs have been investigated to estimate the third-order nonlinear refractive indices. The findings have indicated a considerable enhancement of nonlinear refractive index in $ZnS–Ag_2S$ CSNHs in comparison to pristine ZnS NPs. Finally, both samples of Pristine–ZnS and $ZnS–Ag_2S$ CSNHs have presented self-defocusing effects due to negative refractions under a radiation of 1064 nm.

References

1. T. Ning, Y. Zhou, H. Shen, H. Lu, Z. Sun, L. Cao, D. Guan, D. Zhang, G. Yang, Appl. Surf. Sci. **254**, 1900 (2008)
2. M. Yue, J. Si, L. Yan, Y. Yu, X. Hou, Opt. Mater. Express **8**, 698 (2018)
3. M.Y. Han, W. Huang, C.H. Chew, L.M. Gan, X.J. Zhang, W. Ji, J. Phys. Chem. B **102**, 1884 (1998)
4. A. Azmand, H. Kafashan, J. Alloys Compd. **779**, 301 (2019)
5. C. Wang, L. Guan, Y. Mao, Y. Gu, J. Liu, S. Fu, Q. Xu, J. Phys. D **42**, 45403 (2009)
6. G.S. Thool, M. Baid, A.K. Singh, N.P. Singh, Mater. Today Proc. **5**, 15285 (2018)
7. K. Vijai Anand, G. Vinitha, M. Karl Chinnu, R. Mohan, R. Jayavel, J. Nonlinear Opt. Phys. Mater. **24**, 1550016 (2015)
8. T.D. Krauss, F.W. Wise, Appl. Phys. Lett. **65**, 1739 (1994)
9. J.W.M. Chon, P. Zijlstra, M. Gu, J. van Embden, P. Mulvaney, Appl. Phys. Lett. **85**, 5514 (2004)
10. K. Liu, J. Li, Q. Liu, M. Meng, L. Hu, C. Xu, J. Alloys Compd. **718**, 122 (2017)
11. M.C. Divyasree, N.K.S. Narendran, K. Chandrasekharan (eds.), *Recent Trends in Materials Science and Applications* (Springer, Cham, 2017), pp. 171–178
12. J. Kaur, A. Gupta, O.P. Pandey, Sol. Energy **176**, 678 (2018)
13. J. Xue, J. Liu, S. Mao, Y. Wang, W. Shen, W. Wang, L. Huang, H. Li, J. Tang, Mater. Res. Bull. **106**, 113 (2018)
14. S. Lin, Y. Feng, X. Wen, P. Zhang, S. Woo, S. Shrestha, G. Conibeer, S. Huang, J. Phys. Chem. C **119**, 867 (2014)
15. P.K. Tkm, A.K. Sk, Photochem. Photobiol. Sci. **18**, 148 (2019)
16. T.S. Kondratenko, A.I. Zvyagin, M.S. Smirnov, I.G. Grevtseva, A.S. Perepelitsa, O.V. Ovchinnikov, J. Lumin. **208**, 193 (2019)
17. Y.L. Chueh, C.H. Hsieh, M.T. Chang, L.J. Chou, C.S. Lao, J.H. Song, J.Y. Gan, Z.L. Wang, Adv. Mater. **19**, 143 (2007)
18. M. Dehghanipour, M. Khanzadeh, M. Karimipour, M. Molaei, Opt. Laser Technol. **100**, 286 (2018)
19. L. Liu, S. Hu, Y. Dou, T. Liu, J. Lin, Y. Wang, Beilstein J. Nanotechnol. **6**, 1781 (2015)
20. M. Liu, Z. Xu, B. Li, C. Lin, D. Bai, N. Shan, W. You, Mater. Lett. **65**, 555 (2011)
21. T.V. Murzina, I.A. Kolmychek, J. Wouters, T. Verbiest, O.A. Aktsipetrov, JOSA B **29**, 138 (2012)
22. V. Kumari, V. Kumar, B.P. Malik, R.M. Mehra, D. Mohan, Opt. Commun. **285**, 2182 (2012)
23. M.R. Sharifimehr, K. Ayoubi, E. Mohajerani, Opt. Mater. **49**, 147 (2015)
24. J.L.J. Pérez, R. Gutiérrez-Fuentes, J.F.S. Ramírez, O.U.G. Vidal, D.E. Téllez-Sánchez, Z.N.C. Pacheco, A.C. Orea, J.A.F. García, Adv. Nanoparticles **2**, 223 (2013)
25. D.A. Reddy, R. Ma, M.Y. Choi, T.K. Kim, Appl. Surf. Sci. **324**, 725 (2015)
26. M. Kuppayee, G.K.V. Nachiyar, V. Ramasamy, Appl. Surf. Sci. **257**, 6779 (2011)
27. B.S.R. Devi, R. Raveendran, A.V. Vaidyan, Pramana **68**, 679 (2007)
28. I. Parvaneh, S. Samira, N. Mohsen, Chinese Phys. B **24**, 46104 (2015)
29. M. Shakouri-Arani, M. Salavati-Niasari, Spectrochim. Acta A **133**, 463 (2014)
30. Y.-P. Zhang, W. Liu, B.-D. Liu, R.-M. Wang, Rare Met. **33**, 1 (2014)
31. W.G. Becker, A.J. Bard, J. Phys. Chem. **87**, 4888 (1983)
32. D. Vasudevan, R.R. Gaddam, A. Trinchi, I. Cole, J. Alloys Compd. **636**, 395 (2015)
33. H. Zhang, B. Wei, L. Zhu, J. Yu, W. Sun, L. Xu, Appl. Surf. Sci. **270**, 133 (2013)
34. L. Zhang, M. Jaroniec, Appl. Surf. Sci. **430**, 2 (2018)
35. R. GhoshChaudhuri, S. Paria, J. Phys. Chem. C **117**, 23385 (2013)
36. F. Zakerian, H. Kafashan, Superlattices Microstruct. **124**, 92 (2018)
37. D. Shao, H. Sun, G. Xin, J. Lian, S. Sawyer, Appl. Surf. Sci. **314**, 872 (2014)
38. S. Mathew, B.S. Bhardwaj, A.D. Saran, P. Radhakrishnan, V.P.N. Nampoori, C.P.G. Vallabhan, J.R. Bellare, Opt. Mater. **39**, 46 (2015)
39. M. Karimipour, M. Ebrahimi, Z. Abafat, M. Molaei, Opt. Mater. **57**, 257 (2016)